https://doi.org/10.1016/j.jmst.2022.05.035

A comparative study on microstructure, nanomechanical and corrosion behaviors of AlCoCuFeNi high entropy alloys fabricated by selective laser melting and laser metal deposition

Yaojia Ren [a], Hong Wu [a], Bin Liu [a], Yong Liu [a], Sheng Guo [b], Z.B. Jiao [c], Ian Baker [d]

a. State Key Laboratory of Powder Metallurgy, Central South University, Changsha 410083, China
b. Department of Industrial and Materials Science, Chalmers University of Technology, Gothenburg SE-41296, Sweden
c. Department of Mechanical Engineering, The Hong Kong Polytechnic University, Hong Kong 999077, China
d. Thayer School of Engineering, Dartmouth College, Hanover NH 03755-8000, United States

Abstract

The present study investigated the microstructure, nanomechanics, and corrosion behavior of AlCoCuFeNi high entropy alloys fabricated by selective laser melting (SLM) and laser metal deposition (LMD). The microstructure of SLM specimens was mainly composed of columnar-grained BCC matrix (~90 μm in width) and Cu-rich twinned FCC phase. The columnar grains grew epitaxially along the building direction and exhibited a strong {001} texture. In comparison, a coarse columnar-grained BCC matrix (~150 μm in width) with a strong <001> texture, rod-like B2 precipitates, and large core-shell structured FCC phases were formed in the LMD specimens due to the high heat accumulation. Consequently, the LMD specimens showed a lower hardness, wear resistance, and corrosion resistance, but higher creep resistance and reduced Young's modulus than the SLM specimens . Hot cracks occurred in both types of specimens, which could not be completely suppressed due to the Cu segregation.

Keywords: Selective laser melting; laser metal deposition; high entropy alloys; nanomechanics; corrosion.

1. Introduction

High-entropy alloys (HEAs) have become a new research frontier in the field of metallic materials due to their promising properties, such as high hardness and superior wear and corrosion resistance [1-3]. The high entropy of mixing of these materials contributes to the stabilization of solid solutions, typically based on simple face-centered cubic (FCC), body-centered cubic (BCC), or hexagonal close-packed (HCP) structures [4-6]. By varying the content of some specific elements, the phase and microstructure of HEAs can be tailored to obtain the desired performance. For instance, when increasing the Cu content (an FCC phase stabilizer) in $CoCrCu_xFeMnNi$, the phase constitution changes from single FCC phase to a mixture of two FCC phases, improving the hardness and yield strength [7]. It has been shown that Cu has a positive effect on mechanical properties of FCC-type HEAs in that dual-phase HEAs can exhibit a good combination of strength and ductility at ambient conditions compared to single-phase HEAs. Inspired by that, a variety of Cu-containing dual-phase HEAs (e.g., AlCoCuFeNi, AlCoCrCuFeNi, and CrCuFeMnNi) with good ductility, and oxidation, wear and corrosion resistance have been developed [8-12].

Despite the beneficial role played by Cu in some HEA systems, Cu has a strong tendency to segregate due to its positive mixing enthalpy with various alloying elements [13-15]. It is worth noting that the segregation of Cu is thermodynamically favorable at high temperatures, which means that the macro-segregation cannot be easily eliminated by heat treatments. Cu-rich FCC phases form via atomic diffusion given a sufficiently high temperature and slow cooling rate [16, 17]. Although arc melting (repeating at least 5 times) or magnetron sputtering (forming thin films) could suppress the macro-segregation of Cu, they have cost-efficiency limitations, especially for producing materials with large-scale and geometrically complex structures [18, 19]. Before adopting the laser additive manufacturing technology with an extremely high cooling rate (10^4-10^8 K/s) [20], it was difficult to balance the microstructural homogeneity and the rapid formability of Cu-containing HEAs.

Laser additive manufacturing, a novel technology that emerged in the past decades, can be categorized into two main types: selective laser melting (SLM) based on powder bed fusion and laser metal deposition (LMD) based on coaxial laser deposition [21-25]. Due to the wide range of critical factors, such as spot size, powder distribution, and layer thickness, these two methods exhibit different thermal histories. For instance, the cooling rate of SLM is 2 to 3 orders of magnitude higher than that of LMD [26, 27]. Therefore, compared to LMD, the materials fabricated by SLM generally have finer grain sizes with resultant superior properties [28]. Nevertheless, these advantages of SLM come at the cost of limited types of materials that can be processed, since cracking along the building direction, due to the large temperature gradient, is commonly seen in SLM-processed materials [29, 30]. The main advantages of LMD, on the other hand, are being able to form various materials with few cracks and to produce large-scale (>1 m) components [31, 32]. Therefore, the selection of forming processes has become a new issue, especially regarding HEAs containing multiple-principal elements, which are highly sensitive to the thermal history [33, 34].

This work aims to compare the segregation behavior of Cu as well as the relationship between the microstructural evolution and properties of AlCoCuFeNi, a Cu-containing HEA, prepared by SLM and LMD. The phase constitution, elemental segregation, microstructural evolution, nano-mechanics, and corrosion behavior of SLM- and LMD-processed AlCoCuFeNi are investigated in detail.

2. Materials and methods

The average particle sizes of the pre-alloyed equiatomic AlCoCuFeNi powders used for SLM and LMD are ~30 and ~100 μm, respectively. The SLM specimens were processed using a FS121M machine (Farsoon Inc., China) under high-purity argon (oxygen content less than 100 ppm); an island scanning strategy was adopted, with a laser power of 200 W, a scan speed of 1 m/s, a hatch spacing of 80 μm, and a layer thickness of 40 μm. The LMD specimens were processed with a LDM2000-60 facility (Laserline, German) using a 0° rotation scanning strategy, Ar as the shielding gas with a flow rate of 25 L/min. The deposition parameters of LMD comprised a laser power of 800 W, a scan speed of 1 m/s, a hatch spacing of 1 mm, and a layer thickness 0.4 mm.

Prior to various characterizations, all specimens were mechanically ground and polished, finishing with a solution containing 90% standard colloidal silica suspension with a particle size of 0.04 μm (OP-S NonDry) and 10 vol.% H_2O_2. The phases present in two types of specimens were analyzed using an X-ray diffractometer (XRD, D/MAX-2500) with Cu-Kα radiation (1.5406 Å). The scanning angle (2θ) covered 20° to 90° at a step size of 0.02°, and the scanning rate was 6°/min. The elemental distribution was checked using an electron probe micro-analyzer (EPMA; JXA-8230, Japan). The microstructure of the specimens was examined using an optical microscope (OM, DM-2700P) and a scanning electron microscope (SEM, Nova NanoSEM 230) equipped with an electron backscatter diffraction (EBSD) detector. The phase constituents were further identified using a transmission electron microscope (TEM, FEI Talos F200x) equipped with a 200 keV energy dispersive spectrometer (EDS).

Nanoindentation measurements were conducted at room temperature using a nanoindenter (UNHT, CSM, Switzerland) equipped with a Berkovich tip. By assuming a Poisson's ratio, $v = 0.3$ [35], the reduced Young's modulus, E_r, was obtained from the load-displacement curve with the maximum indentation load of 30 mN and a dwell time of 15 s. Data from five indentations were collected and averaged for each specimen. The above experimental conditions remained unchanged for the nanoindentation creep tests, except that the holding time was extended from 15 to 600 s. Nano-scratch tests were also carried out along the building direction using the nanoindentation tester, equipped with a Rockwell diamond indenter instead. The chosen loading force and scratch distance were 0.5 N and 200 μm, respectively.

Electrochemical corrosion studies were performed in an aerated 3.5 wt.% NaCl solution in the ambient environment (temperature: 30 °C; humidity: 70%). A Gamry electrochemical workstation equipped with a standard three-electrode system was employed to measure the polarization curves. The open circuit potential (OCP) was measured for 60 min to ensure a steady-state potential, followed by the polarization tests from OCP -0.5 to OCP +0.5 V at a scan rate of 0.166 mV/s.

3. Results

3.1 Phase identification

Figure 1a shows the XRD patterns of the HEA specimens processed by SLM and LMD. The XRD result indicates that the LMD specimen is composed of both BCC and FCC phases, while there is only a weak indication of the FCC phase in the SLM specimen, indicating that the extremely high cooling rate in the SLM process could effectively suppress the formation of the FCC phase, even under the inherent heat treatment (IHT, i.e., thermal cycling caused by subsequent melting) condition [36]. Figures 1b and c present the EBSD phase maps of the two HEA specimens. The phase map of the SLM specimen confirms the presence of the dominating BCC phase, while the fine FCC phase cannot be detected by EBSD using large step sizes. The FCC phase with large sizes in the LMD specimen could be the result of the IHT. It is noted that cracks are seen in the SLM specimen, which will be further discussed in the following sections.

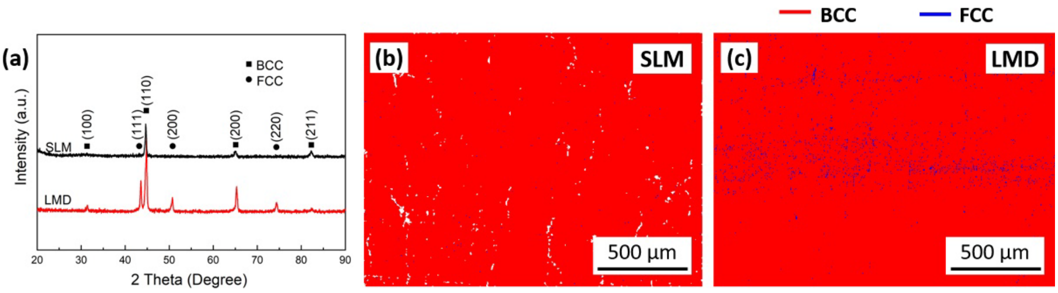

Fig. 1. (a) XRD patterns and (b, c) EBSD phase maps of HEA specimens processed by SLM and LMD, where red and blue represent the BCC and FCC phases, respectively, and white in Fig. 1b points to cracks.

3.2 Microstructure

Figures 2a and b show typical OM images of cross-sections of HEA specimens processed by SLM and LMD. The semi-circular shaped melt pools can be clearly observed in the SLM specimen, as shown in Fig. 2a. Cracks are evident, and the length of cracks in Fig. 2a is larger than the depth of melt pools. These cracks are believed to form due to shrinkage during the solidification process [37]. For the LMD specimen, coarse columnar grains can be observed, as shown in Fig. 2b. The layer thickness is about 400 μm, and the melt pools have a rectangular shape. Together with Fig. 1c, it can be inferred that the formation of the FCC phase inside the heat affected zone (HAZ) is due to the solid-state phase transformation induced by IHT. The low cooling rate in the LMD process allows the melt to backfill and eliminate nano-cracks. However, micro-cracks (widths of ~40μm) caused by shrinkage remain in the materials, as can be seen clearly in Fig.2b.

Figures 2c-f show the secondary electron (SE) images of the HEA specimens processed by SLM and LMD. The semicircular shaped melt pools with a depth of ~50 μm are shown in Fig. 2c, which is larger than the default layer thickness of 40 μm. This means that in addition to the complete melting of fresh powders, the upper part of the previously solidified layer could be re-melted. The observation of coarse precipitates (as marked in Fig. 2c) along the melt pool boundary (MPB) further supports this point. The columnar grains grow from the MPB to the center, along the direction of the heat flow. The solutes are rejected to the front of the solid/liquid interface and then solidified to form the columnar grain boundaries, as shown in Fig. 2e. Apparently, even such a high cooling rate achieved in the SLM specimen fails to suppress the formation of strip-like structures inside the grain. It is noticed that the cracks are formed along the columnar grain boundary, as seen in Fig. 2c. In contrast to SLM, a more uniform temperature gradient can be obtained in the LMD process due to the larger melt pool size. The columnar grains of the LMD specimen are arranged almost in parallel, as shown in Fig. 2d. From Fig. 2f, coarse-sized FCC precipitates along the grain boundary and fine-sized acicular FCC precipitates inside the grain can be observed. This observation further supports that the segregation of solute elements influences the size of the precipitates.

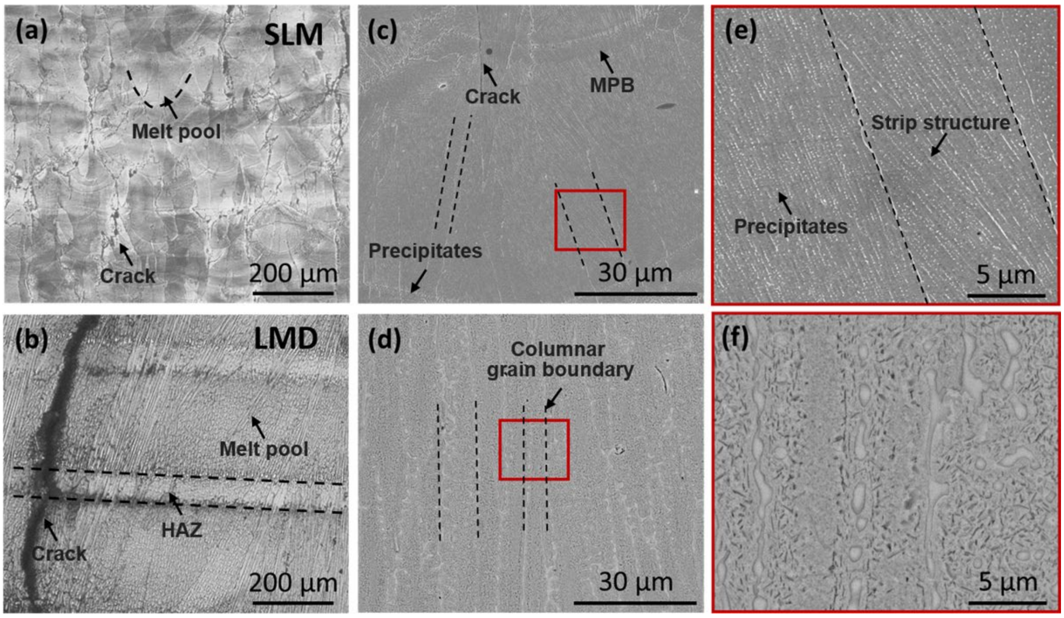

Fig. 2 OM (a, b) and SE (c-f) images from the cross-sections of (a, c, e) SLM and (b, d, f) LMD processed AlCoCuFeNi specimens; (e, f) are the enlarged view of encircled regions in (c, d).

To verify the elemental distribution in SLM- and LMD-processed specimens, back-scattered electron (BSE) images and corresponding X-ray maps of the HEAs are presented in Fig. 3. Cu segregation at the columnar grain boundary and MPB of the SLM specimen could be discerned. The heat accumulation during LMD is more significant than that during SLM due to the lower cooling rate in the former process, which allows for a greater diffusion of solute elements, as seen in Fig. 3b. Combining the XRD and EBSD results, it is reasonable to attribute the formation of the FCC phase in the LMD specimen to the diffusion of Cu, a well-known FCC phase stabilizer. The degree of partitioning for individual elements can be delineated by the partitioning ratio, $\eta = (C_{\text{max}} - C_{\text{min}}) / C_{\text{avg}}$, where C_{max}, C_{min}, and C_{avg} are the maximum, minimum, and average values of the elemental content, respectively. The calculated η values are summarized in Table 1. Since the volume measured using EPMA is only about 1 μm^3, η probably does not accurately reflect the elemental distribution throughout the specimen. Nevertheless, the η values can provide an indication on the tendency of elemental segregation/partitioning in that the higher η value, the higher tendency for partitioning. Table 1 shows that among the five alloying elements, Cu has the highest tendency to segregate. Also, the degree of partitioning in the LMD specimen is higher than that in the SLM specimen.

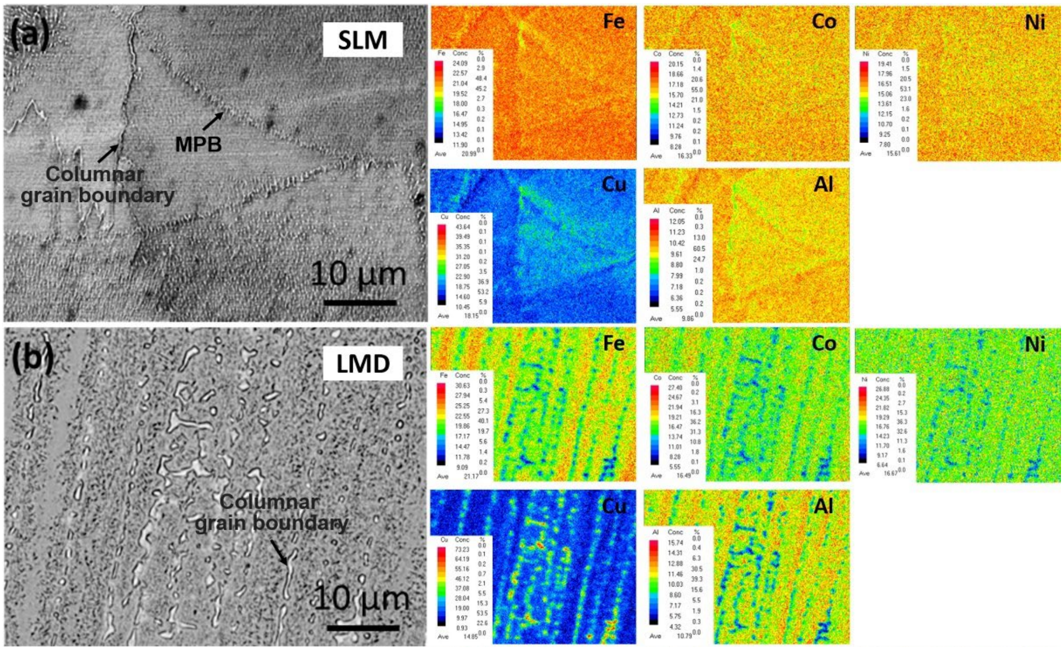

Fig. 3. BSE images and corresponding X-ray maps of the surface of (a) SLM and (b) LMD processed AlCoCuFeNi specimens

Table 1. Partitioning ratios (η) of Al, Co, Cu, Fe, and Ni in the SLM- and LMD-processed specimens.

Partitioning ratio (η)	SLM specimen	LMD specimen
Al	0.66	1.06
Co	0.72	1.33
Cu	1.83	4.80
Fe	0.58	1.02
Ni	0.74	1.21

3.3 EBSD and texture characterization

Figure 4 presents the inverse pole figure (IPF), kernel average misorientation (KAM), and grain boundary orientation maps obtained from the EBSD analysis of SLM and LMD processed specimens. The IPF map of the SLM specimen (Fig. 4a) clearly shows the semicircular shaped melt pools, as marked by dash lines. The columnar grains grow epitaxially, with the width being rather steady, around 90 μm. The laser-induced grain-oriented growth is still displayed on the macro-scale despite the deviation of the local temperature gradient during the SLM processing. As for the LMD specimen, wider columnar grains (~150 μm) with a strong preferred (001) orientation (as shown in Fig. 4d) can be clearly observed. This microstructural difference can be ascribed to the larger spot size, wider melt pool, and lower cooling rate in the LMD process [38]. It is evident that the FCC phase (as marked by arrows) shows different orientations to the BCC matrix.

KAM tells the average misorientation between the orientation in the given grain center and its nearest neighbors, so KAM maps can be used to reveal the local strain distribution. The SLM specimen presents a much higher strain compared to that in the LMD specimen, presumably due to the higher cooling rate in the former. The grain boundary orientation maps of the SLM- and LMD-processed specimens are shown in Figs. 4c and f, respectively. The SLM specimen contains a high fraction (74%) of low-angle grain boundaries (LAGBs), as seen in Fig. 4c. The fraction of LAGBs in the LMD specimen is ~46% in the BCC phase and ~53% in the FCC phase, as shown in the supplementary Fig. S1.

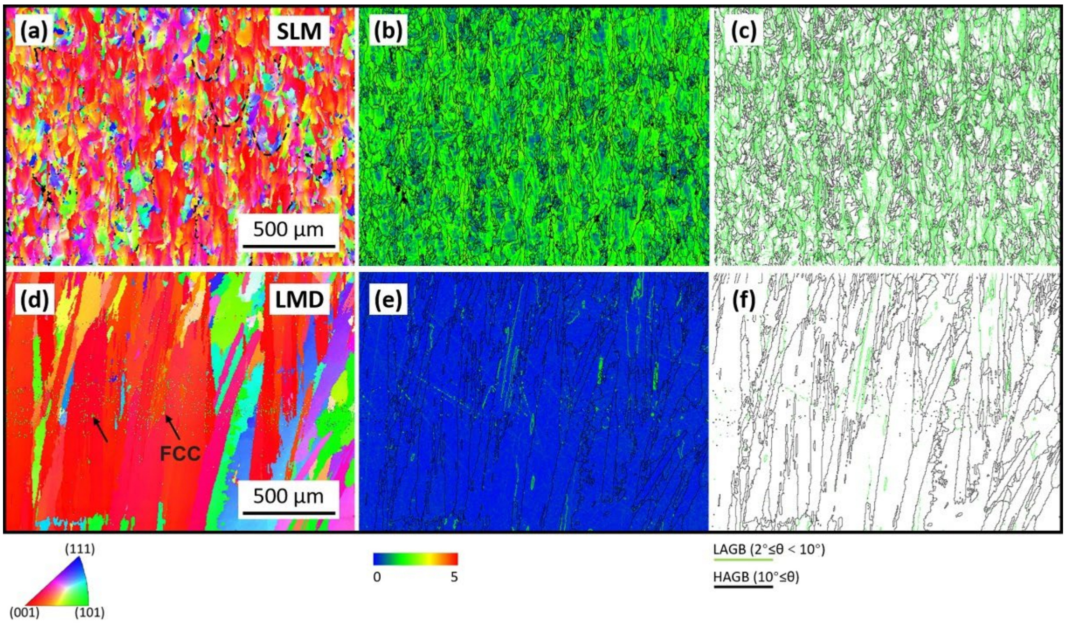

Fig. 4. (a, d) IPF, (b, e) KAM, and (c, f) grain boundary orientation maps of the SLM- and LMD-processed AlCoCuFeNi specimens

The IPF maps shown in Figs. 4a and d show a preferred rather than a random distribution of grain orientations. To further quantify the grain orientations, pole figures (PFs) of the BCC phase in the SLM- and LMD-processed specimens are shown in Fig. 5. It is evident that both specimens exhibit strong {100} textures. The maximum texture indices of the SLM and LMD specimens, calculated using the orientation distribution function (ODF), are 8.31 and 19.23, respectively. The texture strength is an essential parameter for describing the texture intensity, which is the square root of the texture index [39]. The texture strength of the SLM and LMD specimens are 2.33 and 3.26, respectively. Thus, the texture intensity of the LMD specimen is about 1.4 times that of the SLM specimen, suggesting that the thermal history parameters (such as cooling rate, melt pool size, and thermal cycle) have a great effect on the texture development.

The PF for the FCC phase in the LMD specimen is shown in the supplementary Fig. S2. A relatively strong {110} texture with a texture index of 7.55 is presented. Since the (111) plane has the lowest surface energy in the FCC phase, a {111} texture is expected [40]; the {111} to {100} texture transformation could occur in order to reduce the elastic strain energy. Thus, both {111} and {100} textures, in principle, can be expected in the FCC phase. The formation of this {110} texture in the FCC phase can probably be attributed to the transformation from the BCC to FCC phase, following the Bain orientation relationship: $\{001\}_{FCC}$ // $\{001\}_{BCC}$ and $<100>_{FCC}$ // $<110>_{BCC}$ [41].

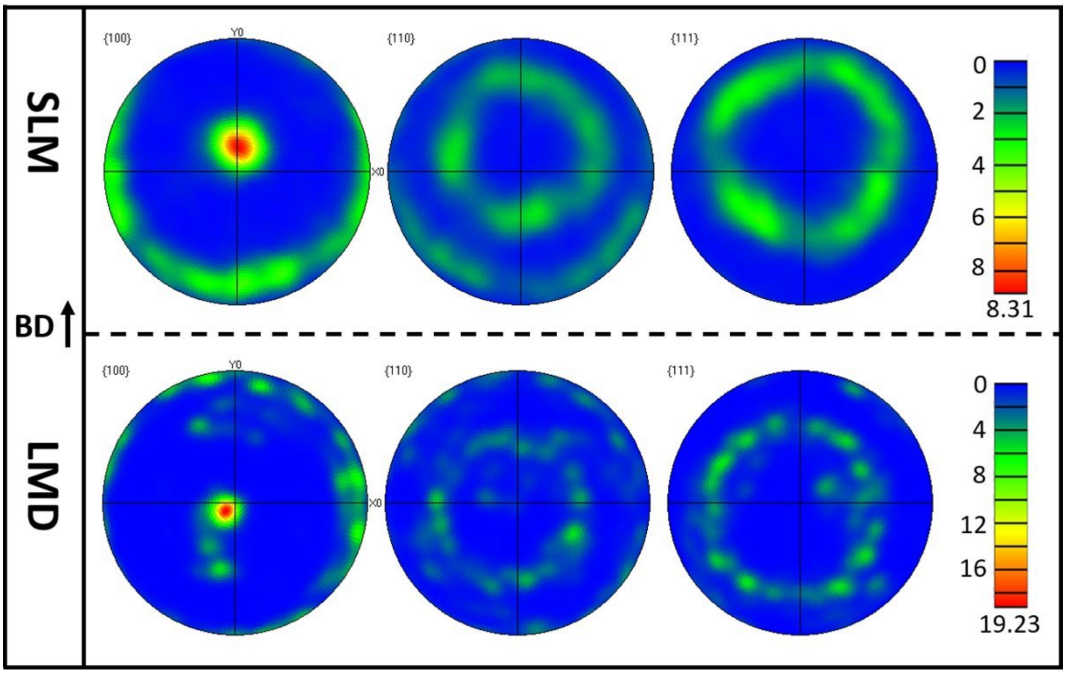

Fig. 5 The pole figures of the BCC phase for the specimens processed by SLM and LMD

3.4 TEM characterization

Figure 6a shows a bright field (BF)-TEM image of the SLM specimen, revealing a columnar grain structure with precipitates along the grain boundaries. The inset shows the selected area electron diffraction (SAED) pattern from the area encircled by the orange square, corresponding to the BCC matrix. Figure 6b is a high-angle annular dark-field (HAADF) image of the area encircled by the red square in Fig. 6a, in which Cu-rich precipitates with sizes of ~110 nm can be observed. The corresponding elemental X-ray maps in Fig. 6d show the clear segregation of Cu and the depletion of Co, Fe and Ni at the columnar grain boundaries. The Cu content in the precipitates can be up to 60 at.% (as characterized by the EDS line analysis shown in Fig. 6b). A high-resolution TEM (HR-TEM) image of the precipitates is shown in Fig. 6c. The inset SAED pattern is from a $\{111\}_{\mathrm{FCC}}$ twin viewed along [011]. In addition, numerous spherical precipitates with a size of ~10 nm can be observed in Fig. 6c, as marked by arrows.

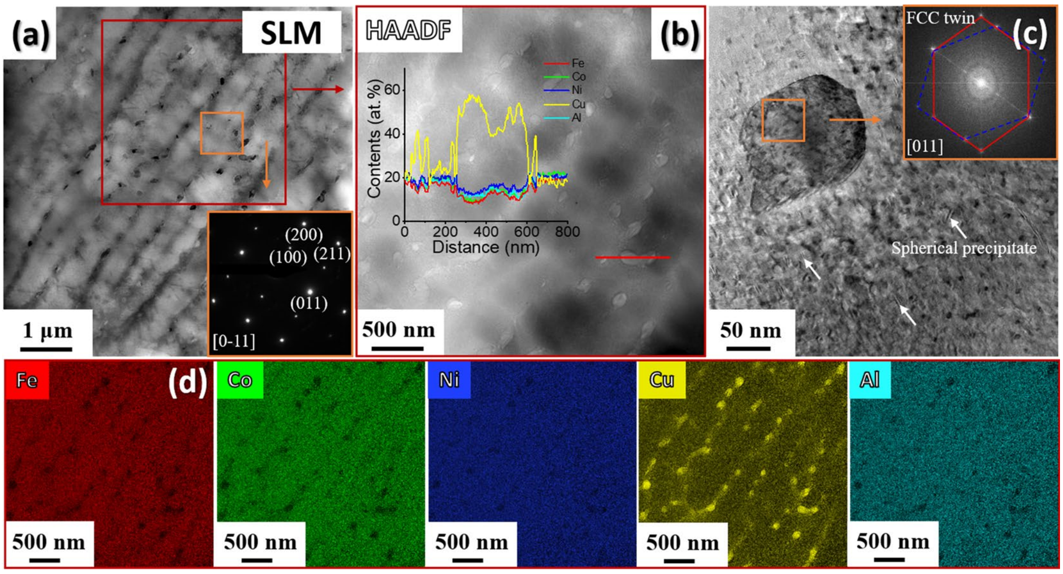

Fig. 6 TEM analysis of the AlCoCuFeNi specimen processed by SLM: (a) BF image, with the inset SAED pattern from the area encircled by the orange square, corresponding to the BCC matrix; (b) an HAADF image for the area encircled by the red square in (a), and EDS line scan results across the marked red line; (c) HR-TEM image of the precipitate, with the inset SAED pattern showing a twinning relation in the FCC phase; (d) X-ray maps of Al, Co, Cu, Fe, and Ni from the area shown in (b).

Figure 7a is a BF-TEM image showing large acicular precipitates in a grain of the LMD specimen. An HAADF image of the marked region is shown in Fig. 7b, while the corresponding elemental X-ray maps of Al, Co, Cu, Fe, and Ni are shown in Fig. 7d. The precipitates are enriched in Cu and depleted in Al. To further quantify the elemental distribution, an EDS line scan was taken across the marked red line shown in Fig. 7b. The Cu enrichment appears at the precipitate-matrix interface, producing a core-shell structure. The Cu-rich shell serves as a buffering layer, which could alleviate the coherency strain and prevent the inter-diffusion between the precipitates and matrix. The latter would lead to a low coarsening rate of the precipitates. A HR-TEM image of the precipitate shown in Fig. 7c also shows this transition layer. The inset SAED pattern from the precipitate confirms its FCC structure, which is consistent with the EBSD result. Away from the transition layer, rod-like precipitates can be discerned. A HAADF image of the rod-like precipitate and the corresponding X-ray maps are shown in Fig. 8. The inset SAED pattern clearly shows the presence of the B2 phase.

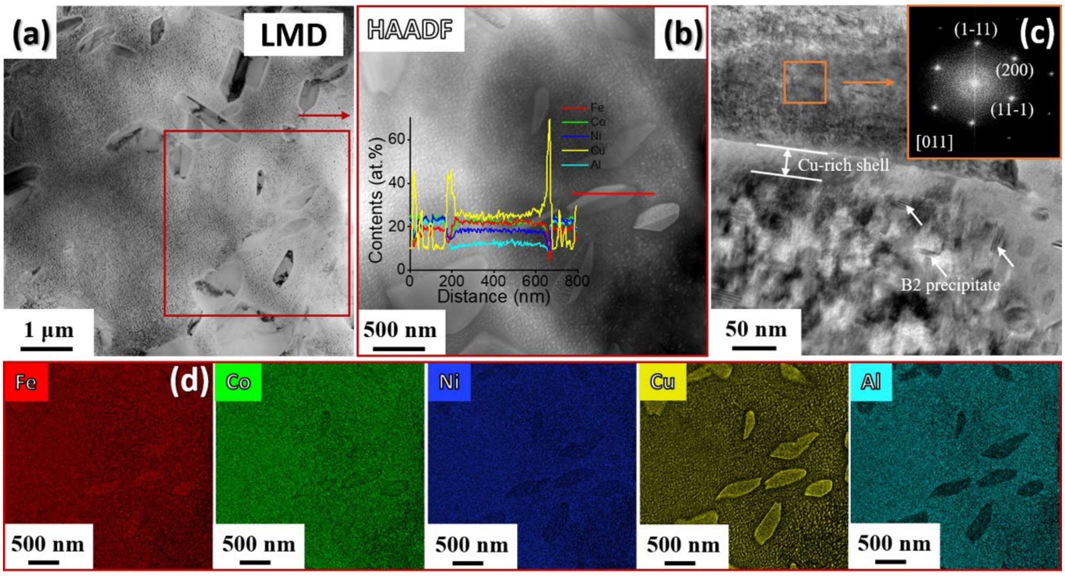

Fig. 7 TEM analysis of the AlCoCuFeNi specimen processed by LMD: (a) BF image; (b) an HAADF image for the area encircled by red lines in (a), and EDS line scan results across the marked red line; (c) HRTEM image of the precipitate, with the inset SAED pattern of FCC phase; (d) X-ray maps of Al, Co, Cu, Fe, and Ni from the area shown in (b).

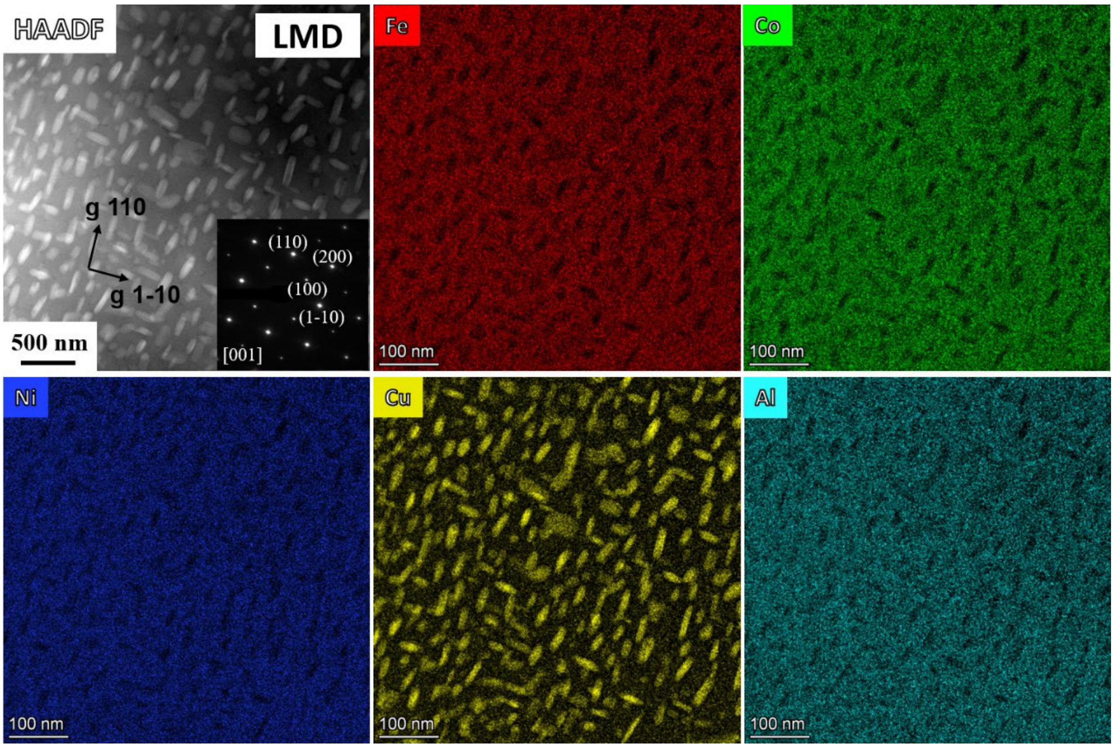

Fig. 8 A HAADF image of rod-like precipitates and the corresponding X-ray maps of Al, Co, Cu, Fe, and Ni. The inset SAED pattern corresponds to the B2 phase.

3.5 Nanomechanical behavior

Figure 9a shows the load-displacement curves of the SLM and LMD specimens. The derived average hardness (H) and reduced Young's modulus (E_r) are shown in Fig. 9b. Compared with the SLM specimen ($H = 761 \pm 26$ HV and $E_r = 143 \pm 5$ GPa), the LMD specimen has a lower H (538 ± 53 GPa) but higher E_r (165 ± 5 GPa).

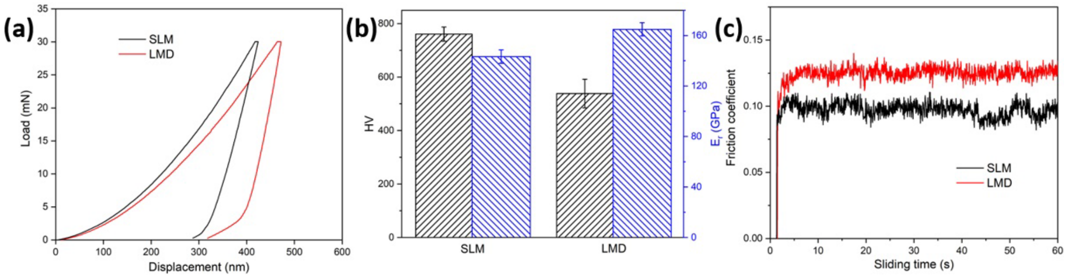

Fig. 9 (a) Load-displacement curves from nanoindentation tests; (b) hardness and E_r values; (c) COF versus sliding time (s).

Wear of materials is a complicated process, which typically requires a long duration of destructive testing. Nano-scratch tests, on the other hand, can reflect the initial stage of the wear process, thereby providing clues to the plastic deformation behavior. The coefficient of friction (COF) for the SLM and LMD specimens can be calculated by the lateral force divided by the normal force. The resultant COF curves as a function of sliding time are shown in Fig. 9c. After the surface of the test pieces get in contact with the indenter, the COF values of the test pieces quickly stabilize. The COF for the SLM specimen is ~0.10 with slight fluctuations. A higher COF (~0.12) can be clearly observed in the LMD specimen, indicating a lower wear resistance.

SE images of the scratched surfaces of the SLM and LMD specimens are shown in Figs. 10a and b. The same scratched length of 200 μm was used. Higher magnification images show that the average width of the scratches on the SLM and LMD specimens are about 13.20 and 14.00 μm, respectively. This means that the wear resistance of the SLM specimen is slightly better than that of the LMD specimen, in agreement with the COF results. The existence of grooves suggests that the wear mechanism is dominated by abrasive wear at the initial stage.

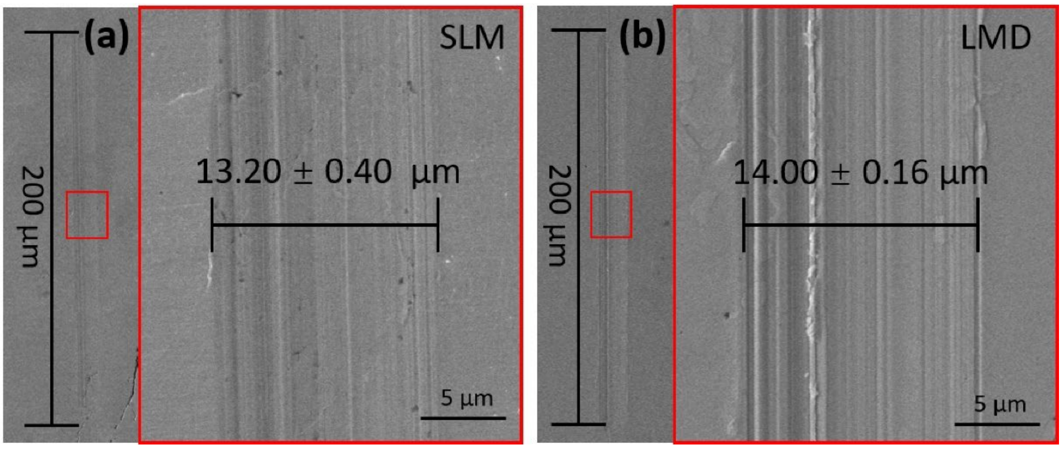

Fig. 10 SE images of the scratched surface for the (a) SLM- and (b) LMD-processed specimens.

The creep deformation induced by a long-time exposure to a static load is an irreversible process related to time. The creep deformation mechanism can be inferred from the stress exponent. The typical creep displacement-time curves of the SLM and LMD specimens are shown in Fig. 11a. The power law relation between the strain rate and stress can be written as follows [42]:

$$\dot{\varepsilon} = C\sigma^n \quad (1)$$

where *C* is a constant, and *n* refers to the stress exponent. The methods to obtain the strain rate and the stress from nanoindentation tests are described elsewhere [43]. From Eq. (1), *n* can be evaluated from the slope of the ln(strain rate)-ln(stress) plot. Figure 11b shows the corresponding ln(strain rate)-ln(stress) plot of the SLM and LMD specimens. The *n* values in the steady-state creep of the SLM and LMD specimens are evaluated to be around 14 and 20, respectively.

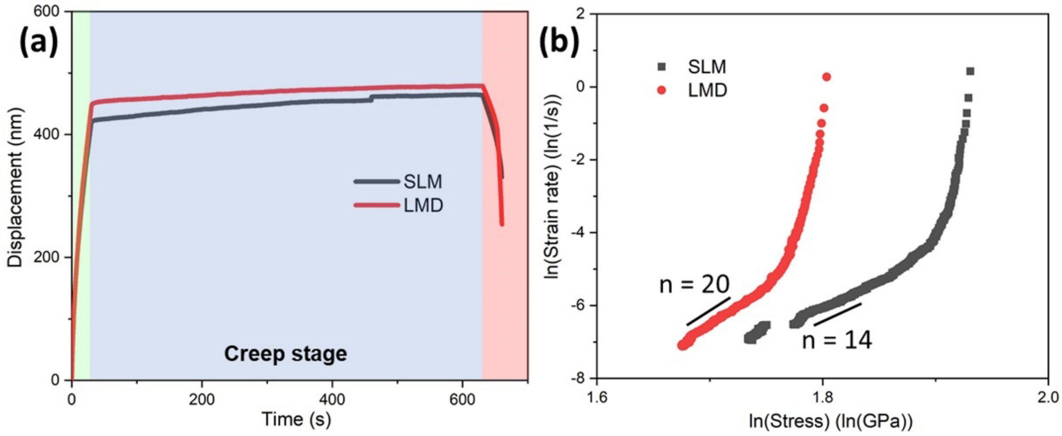

Fig. 11 (a) Creep displacement-time curves; (b) ln(strain rate) versus ln(stress) plots of the SLM and LMD processed specimens.

3.6 Corrosion behavior

The SLM- and LMD-processed AlCoCuFeNi specimens were subjected to OCP tests in a 3.5 wt.% NaCl solution. The alloy surface reached a steady state after immersion for 3600 s in the electrolyte, as shown in Fig. 12a. The potentiodynamic polarization curves of the specimens are shown in Fig. 12b. The corrosion current density (i_{corr}) and corrosion potential (E_{corr}) were acquired from the polarization curves using the Tafel extrapolation method. Fitting parameters including i_{corr}, anodic Tafel slop (β_{a}), cathodic Tafel slop (β_{c}), pitting potenial (E_{pit}) and polarization resistance (R_{p}) are listed in Table 2. The corrosion rate (CR, in mm/year) can be calculated from [44]:

$$CR = 3.27 \times 10^{-3} i_{corr} E_{\mathrm{w}} \rho^{-1} \qquad (2)$$

where i_{corr} is defined as the total anodic current (I_{corr}) divided by the area (μA cm^{-2}), E_{w} is the equivalent weight in grams, and ρ is the density in g/cm^3. The CR_{cor} values of the SLM and LMD specimens are 0.71×10^{-4} and 2.7×10^{-4} mm/y, respectively. When the specimens were immersed in the solution, corrosion preferentially attacked the Cu-rich regions, as shown in the supplementary Fig. S3. This observation indicates that the specimen with less Cu segregation generally has better corrosion resistance.

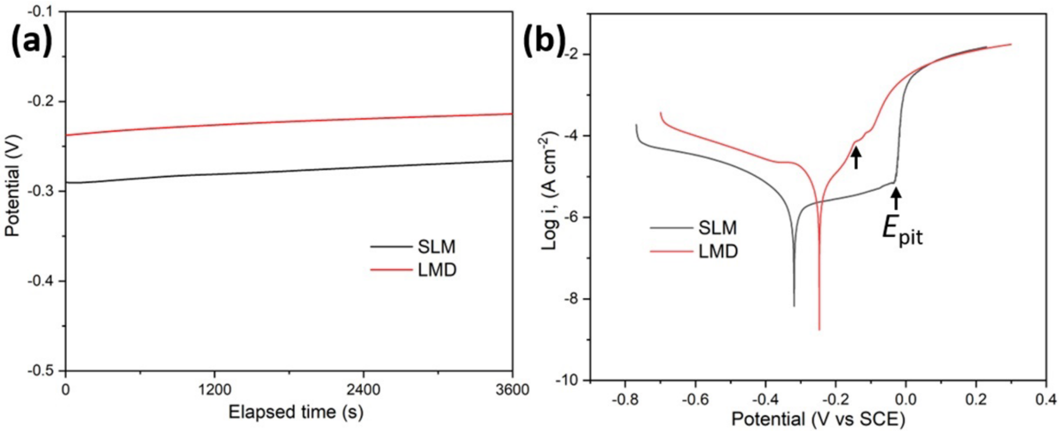

Fig. 12. (a) Open circuit potential (OCP) as a function of time and (b) potentiodynamic polarization curves for the SLM- and LMD-processed AlCoCuFeNi specimens in a 3.5 wt.% NaCl solution at room temperature.

Table 2. Fitting results from polarization curves for the SLM- and LMD-processed AlCoCuFeNi specimens in a 3.5 wt.% NaCl solution. E_{corr}: corrosion potential, i_{corr}: corrosion current density, β_a: anodic Tafel slope, β_c: cathodic Tafel slope, E_{pit}: pitting potenial and R_p: polarization resistance.

Specimens	E_{corr} (V)	i_{corr} (μA cm^{-2})	β_a (V dec^{-1})	β_c (V dec^{-1})	E_{pit} (V)	R_p (Ω cm^2)
SLM	-0.31	0.86	9.77	-13.98	-0.03	2.91×10^6
LMD	-0.25	3.25	12.88	-15.16	-0.14	0.93×10^6

4. Discussion

4.1 Microstructure evolution

The spot size of the LMD process is about 120 µm, which is 2 times larger than that of the SLM process, contributing to the formation of columnar grains with a width of ~150 µm in the LMD specimen, comparing to ~a width of 90 µm in the SLM specimen. Although the extremely high cooling rate (10^6 K/s) in the SLM process was shown to suppress the Cu macro-segregation, the partitioning of Cu in the nanoscale still occurred due to its positive enthalpy of mixing with Fe, Co, and Ni. The strong temperature gradient in the SLM specimen induced localized Marangoni flow, which led to the formation of strip-like structures after solidification (Fig. 2e). The formation of these twinned FCC phases is probably attributed to the solid-solid phase transformation induced by IHT. That is, the Cu-rich twined FCC phase originates from the BCC matrix. Similarly, the formation of core-shell FCC phase could also be related to IHT.

To ensure a sufficient energy input per unit area, the laser power of the LMD process needs to be larger than that of the SLM process, which results in a relatively low cooling rate and high heat accumulation in the LMD process. Thus, the LMD specimen can be regarded as the annealed SLM specimen to some extent. To keep the low total free energy, the twinned Cu-rich phase eventually grows to core-shell structured FCC phase. It is worth noting that there is little internal strain in the LMD specimen (Fig. 4e). Similar results have been reported in LMD CoCrFeNi and AlCoCrFeNi HEAs [45-47]. Compared with the SLM specimen, the LMD specimen is subject to more *in-situ* annealing treatments, which can relax the internal stress induced by rapid cooling. However, an increase in the precipitate size is doomed to occur. The HAGBs, especially those with the misorientation greater than 45°, have shown their ability to prevent or to deflect cracks during their propagation [48]. Only 5% of HAGBs have the misorientation greater than 45° in the SLM specimen, which is in contrast with 11% in the BCC phase and 32% in the FCC phase in the LMD specimen. Again, this implies that the formation of the Cu-rich FCC phase in the LMD specimen is beneficial to suppress nano-cracks. Unfortunately, the low melting point liquid films formed by severe segregation of Cu in the LMD process are prone to crack and form macro-cracks (Fig. 2b) during the solidification shrinkage.

4.2 Nanomechanical and corrosion behaviors

Young's modulus exhibits an orientation-dependence, i.e., a higher Young’s modulus is expected along the close-packed direction in cubic crystals [49]. Since the close-packed direction of BCC crystals is <111>, the stronger {100} texture in the LMD specimen would suggest a lower Young’s modulus compared to that in the SLM specimen. However, the measured E_r of the LMD specimen is even higher than that of the SLM specimen. The enhancement of E_r in the LMD specimen should mainly be attributed to the formation of the core-shell structured FCC phases. The close-packed direction of FCC crystals is <110>, so that the core-shell structured FCC phase with a strong {110} texture leads to a higher E_r. The finer size of columnar grains and precipitates in the SLM specimen can provide higher hardness owing to the Hall-Petch effect. LAGBs are capable of hindering the movement and migration of dislocations, being able to adapt to the sever plastic deformation in the limited volume [50]. The strengthening effect of LAGBs has been observed in the SLM-processed 316L alloys [51], which is believed to contribute to the high hardness of the SLM specimens in this work. Hardness and reduced Young’s modulus, as two critical indicators regarding the resistance to plastic deformation, are closely related to the wear resistance of materials. Generally, a high hardness and low reduced Young’s modulus are desirable for the good wear resistance, which can be reflected from the narrow scratch widths in the SLM specimen. The creep mechanism is dominated by the dislocation movement in the case of $n > 3$ [52]. The high stress exponents in the SLM- and LMD-processed specimens indicate a high level of dislocation-precipitate interactions. The dislocation motion might be pinned by the nano-sized precipitates, which restrains the plastic deformation during the creep process [53]. It can be inferred that the higher n value (i.e., better creep resistance) in the LMD specimen is due to the larger size of the rod-like precipitates.

Compared with the LMD specimen, the wider passivation region of the SLM specimen indicates that a stable surface passive film can form even when nano-cracks are present. It has been confirmed that the pitting susceptibility in the chloride solution is related to the crystallographic orientation, e.g., the (100) plane exhibits good pitting resistance owing to its high surface energy [54]. However, the continuous micro-cracks along the building direction in the LMD specimen provide the corrosion channels for the electrolyte to penetrate the specimen, resulting in a narrow passivation region and low E_{pit}. This accounts for the lower corrosion resistance in the LMD specimen, which is consistent with its higher CR_{cor} values. The micro-cracks facilitated corrosion in the LMD specimen leads to a higher i_{corr} value (Table 2).

For comparison, the hardness and corrosion properties of Cu-containing HEAs from other studies are summarized in Table 3. It can be seen that the specimens in this study have superior hardness combined with good corrosion properties, even though the hot cracks in the SLM and LMD specimens caused by Cu segregation cannot be fully suppressed. The underlying reason is ascribed to the unique hierarchical and heterogeneous microstructures in SLM- and LMD-processed specimens, including the columnar-grained BCC matrix with a strong <001> texture, spherical and rod-like precipitates within the BCC matrix, and high fractions of LAGBs.

Table 3. Hardness and corrosion behavior of various Cu-containing HEAs

Alloys	Preparation	Phase	Hardness (HV)	Solution	E_{corr} (V)	i_{corr} (μA cm^{-2})
AlCoCuFe$_{2.1}$Ni [14]	GTA	BCC + FCC	407	3.5 wt% NaCl	−0.64	8.79
AlCoCuFe$_{2.1}$Ni [14]	U-GTA	BCC + FCC	468	3.5 wt% NaCl	−0.45	6.31
CoCrCuFeNi [55]	PTA	FCC	195	6 N HCl	-0.4	1.1×10^2
CoCrCuFeNbNi [55]	PTA	FCC + Laves	350	6 N HCl	-0.4	8.9×10^2
AlCoCuFeNi [56]	AC	BCC + B2 + FCC	391	-	-	-
AlCoCuFeNi [57]	AC	BCC + B2 + FCC	387	0.5 mol/L H_2SO_4	-0.058	7.93
AlCoCuFeNi This work	SLM	BCC + FCC	761	3.5 wt.% NaCl	-0.31	0.86
AlCoCuFeNi This work	LMD	BCC + B2 + FCC	538	3.5 wt.% NaCl	-0.25	3.25

PTA-plasma transferred arc cladding; AC-arc melting; (U-)GTA-(ultrasonic assisted-) gas tungsten arc cladding.

5. Conclusions

AlCoCuFeNi was successfully produced by SLM and LMD. The resulting microstructure, nanomechanical behavior and corrosion behavior were systematically studied. The following conclusions can be drawn:

1. Due to the high cooling rate the SLM-processed specimen consisted of a fine columnar-grained (~90 μm of width) BCC matrix with a strong <001> texture and Cu-rich twinned FCC precipitates. By contrast, the LMD-processed specimen experienced a lower cooling rate, which enabled Cu to diffuse more sufficiently. The LMD specimen consisted of a coarser columnar-grained (~150 μm of width) BCC matrix with a stronger <001> texture, rod-like B2 precipitates, and core-shell structured FCC phases. Hot cracks in both SLM and LMD specimens could not be fully suppressed due to the Cu segregation.

2. The SLM-processed specimens exhibited a higher hardness (761 HV) and lower E_r

(143 GPa) compared to the LMD specimen, which accounted for its better wear resistance. The wear mechanism in both specimens was dominated by the abrasive wear at the initial stage, as revealed from the nano-scratch tests. The creep deformation in both SLM- and LMD-processed specimens involved a high level of dislocation-precipitate interactions.

3. The SLM specimen possessed a lower OCP value (-0.26 V), lower corrosion current density (0.86 μA cm^{-2}), lower corrosion rate (0.71 × 10^{-4} mm y^{-1}), and higher polarization resistance (2.91 × 10^{6} Ω cm^{2}), therefore a better corrosion resistance compared to the LMD specimen. The LMD specimen displayed a narrower passive region (~80 mV) and a lower E_{pit} (-0.04 V) due to the formation of micro-cracks.

Acknowledgements

This work was supported by the Projects of International Cooperation and Exchanges NSFC (Grant No. 52111530193), Key Research and Development Program of Hunan Province (Grant No. 2022SK2006), Fundamental Research Funds for the Central University of Central South University (Grant No. 2021ZZTS0098), and HK Research Grants Council (ECS 25202719 and GRF 15227121) . The authors would also thank Sinoma Institute of Materials Research (Guang Zhou) Co., Ltd. for the assistance with the TEM characterization.

References

[1] Y. Ye, Q. Wang, J. Lu, C. Liu, Y. Yang, High-entropy alloy: challenges and prospects, Materials Today 19(6) (2016) 349-362.

[2] Y. Yang, Y. Ren, Y. Tian, K. Li, W. Zhang, Q. Shan, Y. Tian, Q. Huang, H. Wu, Microstructure and properties of FeCoCrNiMoSi$_x$ high-entropy alloys fabricated by spark plasma sintering, Journal of Alloys and Compounds 884 (2021) 161070.

[3] Y. Yang, Y. Ren, Y. Tian, K. Li, L. Bai, Q. Huang, Q. Shan, Y. Tian, H. Wu, Microstructure and tribological behaviors of FeCoCrNiMoSi$_x$ high-entropy alloy coatings prepared by laser cladding, Surface and Coatings Technology (2021) 128009.

[4] C. Han, Q. Fang, Y. Shi, S.B. Tor, C.K. Chua, K. Zhou, Recent advances on high-entropy alloys for 3D printing, Advanced Materials 32(26) (2020) 1903855.

[5] I.-S. Liu, An overview of entropy principle, Journal of Micromechanics and Molecular Physics (2021) 1-6.

[6] Y. Ren, L. Liang, Q. Shan, A. Cai, H. Wu, Effect of volumetric energy density on microstructure and tribological properties of FeCoNiCuAl high-entropy alloy produced by laser powder bed fusion, Virtual and Physical Prototyping 15(sup1) (2020) 543-554.

[7] X. Xian, L. Lin, Z. Zhong, C. Zhang, C. Chen, K. Song, J. Cheng, Y. Wu, Precipitation and its strengthening of Cu-rich phase in CrMnFeCoNiCu$_x$ high-entropy alloys, Materials Science and Engineering: A 713 (2018) 134-140.

[8] M. Zhang, X. Zhou, D. Wang, L. He, X. Ye, W. Zhang, Additive manufacturing of in-situ strengthened dual-phase AlCoCuFeNi high-entropy alloy by selective electron beam melting, Journal of Alloys and Compounds 893 (2022) 162259.

[9] F.-Y. Cho, S.-W. Tung, F.-Y. Ouyang, High temperature oxidation behavior of high entropy alloy $Al_4Co_3Cr_{25}Cu_{10}Fe_{25}Ni_{33}$ in oxygen-containing atmospheres, Materials Chemistry and Physics 278 (2022) 125678.

[10] Yuan, Yu, Jun, Wang, Jinshan, Li, Hongchao, Kou, Haitao, Duan, Tribological behavior of AlCoCrCuFeNi and AlCoCrFeNiTi$_{0.5}$ high entropy alloys under hydrogen peroxide solution against different counterparts, Tribology International 92 (2015) 203-210.

[11] E. Zhou, D. Qiao, Y. Yang, D. Xu , F. Wang, A novel Cu-bearing high-entropy alloy with significant antibacterial behavior against corrosive marine biofilms, Journal of Materials Science and Technology 46 (2020) 201-210.

[12] S.M. Oh, S.I. Hong, Microstructural stability and mechanical properties of equiatomic CoCrCuFeNi, CrCuFeMnNi, CoCrCuFeMn alloys, Materials Chemistry and Physics (2017) 120-125.

[13] Y. Wen, A. Hirata, Z. Zhang, T. Fujita, C. Liu, J. Jiang, M. Chen, Microstructure characterization of Cu-rich nanoprecipitates in a Fe-2.5 Cu-1.5 Mn-4.0 Ni-1.0 Al multicomponent ferritic alloy, Acta materialia 61(6) (2013) 2133-2147.

[14] Q. Fan, C. Chen, C. Fan, Z. Liu, X. Cai, S. Lin, C. Yang, Ultrasonic Suppression of Element Segregation in Gas Tungsten Arc Cladding AlCoCuFeNi High-entropy Alloy Coatings, Surface and Coatings Technology (2021) 127364.

[15] A. Verma, P. Tarate, A. Abhyankar, M. Mohape, D. Gowtam, V. Deshmukh, T. Shanmugasundaram, High temperature wear in CoCrFeNiCu$_x$ high entropy alloys: the role of Cu, Scripta Materialia 161 (2019) 28-31.

[16] R. Sonkusare, S. Yadav, N. Gurao, K. Biswas, High Entropy Alloys in Bulk Form: Processing Challenges and Possible Remedies, High Entropy Alloys, CRC Press, 2020, 125-168.

[17] Y. Zhang, T.T. Zuo, Z. Tang, M.C. Gao, K.A. Dahmen, P.K. Liaw, Z.P. Lu, Microstructures and properties of high-entropy alloys, Progress in materials science 61 (2014) 1-93.

[18] J. Cieslak, J. Tobola, K. Berent, M. Marciszko, Phase composition of Al_xFeNiCrCo high entropy alloys prepared by sintering and arc-melting methods, Journal of Alloys and Compounds 740 (2018) 264-272.

[19] B. Braeckman, F. Boydens, H. Hidalgo, P. Dutheil, M. Jullien, A.-L. Thomann, D. Depla, High entropy alloy thin films deposited by magnetron sputtering of powder targets, Thin Solid Films 580 (2015) 71-76.

[20] T. Zhang, C.-T. Liu, Design of titanium alloys by additive manufacturing: A critical review, Advanced Powder Materials (2021).

[21] A. Adeyemi, E.T. Akinlabi, R.M. Mahamood, Powder bed based laser additive manufacturing process of stainless steel: A review, Materials Today: Proceedings 5(9) (2018) 18510-18517.

[22] K.O. Abdulrahman, E.T. Akinlabi, R.M. Mahamood, S. Pityana, M. Tlotleng, Laser metal deposition of titanium aluminide composites: A review, Materials Today: Proceedings 5(9) (2018) 19738-19746.

[23] H. Fan, Y. Liu, S. Yang, Martensite decomposition during post-heat treatments and the aging response of near-α Ti-6Al-2Sn-4Zr-2Mo (Ti-6242) titanium alloy processed by selective laser melting (SLM), Journal of Micromechanics and Molecular Physics (2021) 2050018.

[24] J.e. Sun, B. Zhang, X. Qu, High strength Al alloy development for laser powder bed fusion, Journal of Micromechanics and Molecular Physics (2021) 2141001.

[25] M. He, Y. Ni, S. Wang, On the microstructure and tensile properties of Inconel 718 alloy fabricated by selective laser melting and conventional casting, Journal of Micromechanics and Molecular Physics (2021) 2141003.

[26] D. Carluccio, M. Bermingham, D. Kent, A.G. Demir, B. Previtali, M.S. Dargusch, Comparative study of pure iron manufactured by selective laser melting, laser metal deposition, and casting processes, Advanced Engineering Materials 21(7) (2019) 1900049.

[27] D. Karlsson, A. Marshal, F. Johansson, M. Schuisky, M. Sahlberg, J.M. Schneider, U. Jansson, Elemental segregation in an AlCoCrFeNi high-entropy alloy-A comparison between selective laser melting and induction melting, Journal of Alloys and Compounds 784 (2019) 195-203.

[28] J. Zhang, B. Song, C. Cai, L. Zhang, Y. Shi, Tailorable microstructure and mechanical properties of selective laser melted TiB/Ti-6Al-4V composite by heat treatment, Advanced Powder Materials (2021).

[29] R. Li, M. Wang, Z. Li, P. Cao, T. Yuan, H. Zhu, Developing a high-strength Al-Mg-Si-Sc-Zr alloy for selective laser melting: crack-inhibiting and multiple strengthening mechanisms, Acta Materialia 193 (2020) 83-98.

[30] Z. Hu, X. Nie, Y. Qi, H. Zhang, H. Zhu, Cracking criterion for high strength Al–Cu alloys fabricated by selective laser melting, Additive Manufacturing 37 (2021) 101709.

[31] Y. Lee, Y. Bandari, P. Nandwana, B. Gibson, B. Richardson, S. Simunovic, Effect of interlayer cooling time, constraint and tool path strategy on deformation of large components made by laser metal deposition with wire, Applied Sciences 9(23) (2019) 5115.

[32] M. Benoit, S. Sun, M. Brandt, M. Easton, Processing window for laser metal deposition of Al 7075 powder with minimized defects, Journal of Manufacturing Processes 64 (2021) 1484-1492.

[33] Y. Wen, Y. Li, A. Hirata, Y. Zhang, T. Fujita, T. Furuhara, C. Liu, A. Chiba, M. Chen, Synergistic alloying effect on microstructural evolution and mechanical properties of Cu precipitation-strengthened ferritic alloys, Acta materialia 61(20) (2013) 7726-7740.

[34] E. Pickering, R. Muñoz-Moreno, H. Stone, N. Jones, Precipitation in the equiatomic high-entropy

alloy CrMnFeCoNi, Scripta Materialia 113 (2016) 106-109.

[35] M.L. Ali, E. Haque, M.Z. Rahaman, Pressure-and temperature-dependent physical metallurgy in a face-centered cubic NiCoFeCrMn high entropy alloy and its subsystems, Journal of Alloys and Compounds 873 (2021) 159843.

[36] S. Sui, Y. Chew, Z. Hao, F. Weng, C. Tan, Z. Du, G. Bi, Effect of cyclic heat treatment on the microstructure and mechanical properties of laser aided additive manufacturing Ti-6Al-2Sn-4Zr-2Mo alloy, Advanced Powder Materials (2021).

[37] C. Zhang, K. Feng, H. Kokawa, B. Han, Z. Li, Cracking mechanism and mechanical properties of selective laser melted CoCrFeMnNi high entropy alloy using different scanning strategies, Materials Science and Engineering: A 789 (2020) 139672.

[38] M. Moradi, A. Hasani, Z. Pourmand, J. Lawrence, Direct laser metal deposition additive manufacturing of Inconel 718 superalloy: Statistical modelling and optimization by design of experiments, Optics & Laser Technology 144 (2021) 107380.

[39] L. Thijs, M.M. Sistiaga, R. Wauthle, Q. Xie, J.P. Kruth, J.V. Humbeeck, Strong morphological and crystallographic texture and resulting yield strength anisotropy in selective laser melted tantalum, Acta Materialia 61(12) (2013) 4657-4668.

[40] L. Han, L.P. Jeurgens, C. Cancellieri, J. Wang, Y. Xu, Y. Huang, Y. Liu, Z. Wang, Anomalous texture development induced by grain yielding anisotropy in Ni and Ni-Mo alloys, Acta Materialia 200 (2020) 857-868.

[41] A. Singh, T. Hiroto, H. Watanabe, N. Ikeo, T. Mukai, K. Tsuchiya, Phase transformation and morphological features in a cold-worked CrMnFeCoNi high entropy alloy with Al addition, Materials Characterization (2021) 111556.

[42] R. Goodall, T. Clyne, A critical appraisal of the extraction of creep parameters from nanoindentation data obtained at room temperature, Acta materialia 54(20) (2006) 5489-5499.

[43] H. Wu, Y. Ren, J. Ren, L. Liang, R. Li, Q. Fang, A. Cai, Q. Shan, Y. Tian, I. Baker, Selective laser melted AlSi10Mg alloy under melting mode transition: Microstructure evolution, nanomechanical behaviors and tensile properties, Journal of Alloys and Compounds 873 (2021) 159823.

[44] W.H. Ailor, Handbook on corrosion testing and evaluation. Symposium on the state of the art in corrosion testing, Toronto, Canada, June 21-26, 1970, John Wiley and Sons, Inc., New York, 1971.

[45] Y. Cai, X. Li, H. Xia, Y. Cui, S.M. Manladan, L. Zhu, M. Shan, D. Sun, T. Wang, X. Lv, Fabrication of laminated high entropy alloys using differences in laser melting deposition characteristics of FeCoCrNi and FeCoCrNiAl, Journal of Manufacturing Processes 72 (2021) 294-308.

[46] Y. Cai, M. Shan, Y. Cui, S.M. Manladan, X. Lv, L. Zhu, D. Sun, T. Wang, J. Han, Microstructure and properties of FeCoCrNi high entropy alloy produced by laser melting deposition, Journal of Alloys and Compounds 887 (2021) 161323.

[47] Y. Cai, L. Zhu, Y. Cui, J. Han, Manufacturing of FeCoCrNi + FeCoCrNiAl laminated high-entropy alloy by laser melting deposition (LMD), Materials Letters 289 (2021) 129445.

[48] X. Qi, P. Huan, X. Wang, H. Di, X. Shen, Q. Sun, Z. Liu, J. He, Study on the mechanism of heat input on the grain boundary distribution and impact toughness in CGHAZ of X100 pipeline steel from the aspect of variant, Materials Characterization 179 (2021) 111344.

[49] Y. Ye, B. Musico, Z. Lu, L. Xu, Z. Lei, V. Keppens, H. Xu, T. Nieh, Evaluating elastic properties of a body-centered cubic NbHfZrTi high-entropy alloy–A direct comparison between experiments and ab initio calculations, Intermetallics 109 (2019) 167-173.

[50] S. Chen, Q. Yu, The role of low angle grain boundary in deformation of titanium and its size effect,

Scripta Materialia 163 (2019) 148-151.

[51] Y.M. Wang, T. Voisin, J.T. McKeown, J. Ye, N.P. Calta, Z. Li, Z. Zeng, Y. Zhang, W. Chen, T.T. Roehling, Additively manufactured hierarchical stainless steels with high strength and ductility, Nature materials 17(1) (2018) 63-71.

[52] S. Chen, W. Li, X. Xie, J. Brechtl, B. Chen, P. Li, G. Zhao, F. Yang, J. Qiao, P.K. Liaw, Nanoscale serration and creep characteristics of $Al_{0.5}CoCrCuFeNi$ high-entropy alloys, Journal of Alloys and Compounds 752 (2018) 464-475.

[53] N. Burbery, G. Po, R. Das, N. Ghoniem, W. Ferguson, Dislocation dynamics in polycrystals with atomistic-informed mechanisms of dislocation-grain boundary interactions, Journal of Micromechanics and Molecular Physics 2(01) (2017) 1750003.

[54] D. Gu, H. Zhang, D. Dai, C. Ma, S. Li, Anisotropic corrosion behavior of Sc and Zr modified Al-Mg alloy produced by selective laser melting, Corrosion Science 170 (2020) 108657.

[55] J. Cheng, X. Liang, B. Xu, Effect of Nb addition on the structure and mechanical behaviors of CoCrCuFeNi high-entropy alloy coatings, Surface and Coatings Technology 240 (2014) 184-190.

[56] C. Liu, W. Peng, C. Jiang, H. Guo, J. Tao, X. Deng, Z. Chen, Composition and phase structure dependence of mechanical and magnetic properties for $AlCoCuFeNi_x$ high entropy alloys, Journal of Materials Science & Technology 35(6) (2019) 1175-1183.

[57] D. Xiao, P. Zhou, W. Wu, H. Diao, M. Gao, M. Song, P. Liaw, Microstructure, mechanical and corrosion behaviors of AlCoCuFeNi-(Cr, Ti) high entropy alloys, Materials & Design 116 (2017) 438-447.